Ab initio study of electronic, magnetic, and spectroscopic properties in *A*- and *B*-site-ordered perovskite $CaCu_3Fe_2Sb_2O_{12}$

Hitoshi Fujii,[1,2] Masayuki Toyoda,[2,3] Hiroyoshi Momida,[3] Masaichiro Mizumaki,[1,2] Shigeru Kimura,[1,2] and Tamio Oguchi[2,3]

[1]*Japan Synchrotron Radiation Research Institute, SPring-8, 1-1-1 Kouto, Sayo-cho, Sayo-gun, Hyogo 679-5198, Japan*

[2]*CREST, Japan Science and Technology Agency, 7, Gobancho, Chiyoda-ku, Tokyo 102-0076, Japan*

[3]*The Institute of Scientific and Industrial Research, Osaka University, 8-1, Mihogaoka, Ibaraki, Osaka 567-0047, Japan*

(Received 26 February 2014; revised manuscript received 4 July 2014; published 25 July 2014)

Electronic structure, magnetism, x-ray absorption spectroscopy (XAS), and x-ray magnetic circular dichroism (XMCD) spectra of *A*- and *B*-site-ordered quadruple perovskite $CaCu_3Fe_2Sb_2O_{12}$ (CCFSO) were studied using first-principles calculations with inclusion of spin-orbit coupling. The calculated XAS and XMCD spectra for Cu and Fe at the $L_{3,2}$ edges were consistent with a recent experiment and indicate ferrimagnetic ordering with antiparallel magnetic moments between Cu and Fe. The magnetic exchange coupling constants were also calculated to clarify the detailed mechanism of the ferrimagnetic ordering in CCFSO. The coupling constants for Cu-Cu, Fe-Fe, and Cu-Fe pairs were found to be moderate ferromagnetic, weak antiferromagnetic, and strong antiferromagnetic, respectively. From the analysis of the calculated density of states and magnetization density, the microscopic origin of the strong antiferromagnetic coupling between Cu and Fe was successfully elucidated by the superexchange mechanism via the Cu($d_{x^2-y^2}$)-O(p_x)-Fe(t_{2g}) exchange path.

DOI: 10.1103/PhysRevB.90.014430 PACS number(s): 75.47.Lx

I. INTRODUCTION

Recently, *A*- and *B*-site-ordered quadruple perovskite $CaCu_3Fe_2Sb_2O_{12}$ (CCFSO) [Fig. 1(a)], which is a ferrimagnetic insulator with Cu-Fe antiferromagnetic coupling with $T_C = 170$ K, has been synthesized at a pressure of 10 GPa and temperature of 1500 K [1]. This new type of perovskite oxide with magnetic Cu and Fe and nonmagnetic Sb is expected to exhibit intriguing magnetic properties compared to those of its parent perovskite oxides.

For example, a double perovskite Ca_2FeSbO_6 (CFSO), which can be regarded as a parent compound of CCFSO, i.e., *A*-site Ca^{2+} cations in CFSO are substituted with Cu^{2+} with 1 : 3 ordering of Ca/Cu cations, is known to exhibit spin frustration associated with spin-glass behavior because of the antiferromagnetic coupling between Fe^{3+} cations, which are on a geometrically frustrated face-centered-cubic sub-lattice. This antiferromagnetic coupling is weak, and the spin-glass transition temperature of CFSO is on the order of a few 10 K due to the long and tilted Fe-O-Sb-O-Fe exchange path [2]. By introducing Cu^{2+} ions into CFSO, however, it is expected that a new magnetic coupling between Cu and Fe will be induced. This coupling must be stronger than the antiferromagnetic coupling between Fe-Fe; therefore, the spin frustration in CFSO can be released [1].

Also, *A*-site-ordered perovskite $CaCu_3Fe_4O_{12}$ (CCFO) can be considered as another parent compound of CCFSO, i.e., Sb occupies half the Fe sites of CCFO in a rock-salt manner. Even though CCFO is a Pauli paramagnetic metal with high-valence Fe^{4+} at room temperature, it becomes a ferrimagnetic insulator with the valence configuration $CaCu_3Fe_2^{3+}Fe_2^{5+}O_{12}$ with Cu-Fe^{3+}(Fe^{5+}) antiferromagnetic and Fe^{3+}-Fe^{5+} ferromagnetic coupling by charge disproportionation (CD) at temperatures below 210 K, represented as $2Fe^{4+} \rightarrow Fe^{3+} + Fe^{5+}$ (Refs. [3,4]). Similarly, it is expected that the nonmagnetic pentavalent Sb^{5+} cations introduced in CCFO will interrupt the delocalization of Fe^{4+}; therefore, ferrimagnetic and insulating behavior with the valence configuration $CaCu_3Fe_2^{3+}Sb_2^{5+}O_{12}$ is possible.

Xiang *et al.* calculated the thermodynamical stabilities and magnetic structure of CCFSO by using the full-potential augmented plane-wave (FLAPW) method and showed that CCFSO is thermodynamically stable at high pressure and has antiferromagnetic Cu-Fe coupling with spin magnetic moments of -0.7 and 4.17 μ_B for Cu and Fe, respectively [5]. However, the detailed mechanism of the magnetic coupling is still unclear. Furthermore, they could not discuss the orbital magnetic moments in CCFSO because the spin-orbit coupling (SOC) was not taken into account in their calculations. Chen *et al.* conducted x-ray absorption spectroscopy (XAS) and x-ray magnetic circular dichroism (XMCD) for Cu and Fe $L_{3,2}$ edges to discuss the spin and orbital magnetic moments of individual ions in CCFSO [1]. They also confirmed antiferromagnetism between Cu and Fe and revealed that the orbital magnetic moment of Cu is small but non-negligible in comparison with the spin magnetic moment due to the uniaxial symmetry of the CuO_4 square planes [see Fig. 1(b)], even for the weak SOC system.

In this paper, we discuss the electronic structure and magnetic properties of CCFSO based on the density functional theory (DFT) with inclusion of SOC as well as Hubbard *U* parameters. We also calculate XAS and XMCD spectra for Cu $L_{3,2}$, Fe $L_{3,2}$, and O *K* edges within a one-electron picture to directly compare with the experimental spectra. The magnetic exchange coupling constants for Cu-Cu, Fe-Fe, and Cu-Fe pairs are also calculated to clarify the detailed mechanism of the ferrimagnetic order in CCFSO.

II. METHODS

Based on DFT first-principles electronic structure, calculations are done within the generalized gradient approximation (GGA) using the Perdew-Burke-Ernzerhof scheme [6,7]. We use the HiLAPW code, which is based on the all-electron FLAPW method [8]. We use a second-variation procedure to include SOC in addition to a scalar-relativistic scheme, which gives accurate description equivalent to solving the Dirac

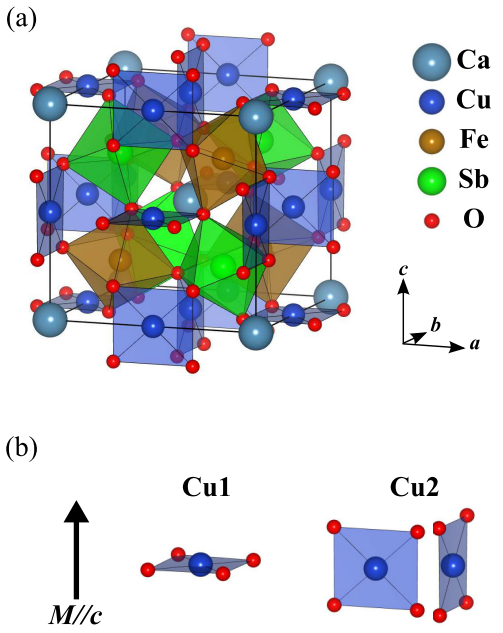

FIG. 1. (Color online) (a) Crystal structure of $CaCu_3Fe_2Sb_2O_{12}$ (CCFSO). CCFSO is a ferrimagnetic insulator with $Pn\bar{3}$ cubic symmetry consisting of CuO_4 square planes and largely tilted FeO_6 and SbO_6 octahedra with Fe-O-Sb angle of 138.5°. (b) Nonequivalent CuO_4 square planes under magnetization along the [001] direction. Cu1 (Cu2) indicates Cu in perpendicular (parallel) plane to magnetization axis.

equation. The GGA + U method is used to properly take into account the strong correlation effects in the 3d transition-metal oxides with the effective parameter $U_{\rm eff} = U - J$, where $U(J)$ is the Coulomb (exchange) part of the electron-electron interaction. We choose $U_{\rm eff} = 7.0$ and 4.0 eV for Cu and Fe d states, respectively, which give the correct results for all properties in CCFO [9,10]. The plane-wave expansion cutoffs are 20 Ry for wave functions and 160 Ry for charge density and potential functions. The muffin-tin sphere radii (and the valence electrons) are chosen as 1.1, 1.0, 1.0, 1.0, and 0.8 Å for Ca($3p^6 4s^2$), Cu($3d^{10}4s^1$), Fe($3d^6 4s^2$), Sb($4d^{10}5s^2 5p^3$), and O($2s^2 2p^4$), respectively. For the Brillouin-zone integration, an 8 × 8 × 8 mesh is used with the tetrahedron integration technique. The crystal structure determined at 300 K is used for the calculation and the lattice relaxation is not taken into account because the difference between the experimental [1] and optimized structure [5] is very small, which is the general feature of ordered perovskites [11].

The XAS intensities $I_h(\omega)$ for a polarized incident x-ray with helicity ($h = +, -$, or 0) and a photon energy $\hbar\omega$ can be described by Fermi's golden rule for the transition probability from initial core states $|i\rangle$ to final unoccupied-band states $|f\rangle$,

$$I_h(\omega) = \frac{2\pi}{\hbar} \sum_{i,f} |\langle f|F_h|i\rangle|^2 \delta(\epsilon_f - \epsilon_i - \hbar\omega), \qquad (1)$$

within the one-electron picture, where ϵ_i (ϵ_f) is the eigenenergy of the initial (final) state and F_h is the electron-photon interaction operator. In our calculation based on the FLAPW method, the transition matrix elements are calculated only within the muffin-tin spheres where the initial and final states are expanded in terms of spherical wave functions with angular momentum and spin (l, m, and m_s). Within the electric dipole approximation, F_h can be written using the spherical harmonics $Y_{lm}(\hat{r})$ as

$$F_h = \sqrt{\frac{4\pi}{3}} er E_h Y_{1h}, \qquad (2)$$

where $E_\pm = \mp(E_x \mp iE_y)/\sqrt{2}$ and $E_0 = E_z$ are the photon electric fields with helicity. In this way, the matrix elements $\langle f|F_h|i\rangle$ are calculated inside the corresponding muffin-tin spheres. The XMCD spectra, which show the difference in the XAS spectra between right-handed ($h = +$) and left-handed ($h = -$) circularly polarized incident light, are also calculated to compare with and understand the experimental data. The core-hole potential in the final states is neglected in our calculations. The calculated spectra are broadened using the Lorentzian function with $\gamma = 0.4$, 0.4, and 0.14 eV for Cu, Fe, and O, respectively [12], to take into account the experimental core-hole lifetime broadening. Our formulation for calculating XAS and XMCD spectra with the FLAPW method has been successfully applied to several transition-metal compounds [10,13–15].

The magnetic exchange coupling constants for Cu-Cu, Fe-Fe, and Cu-Fe pairs are estimated by the constrained DFT calculations with noncollinear spin orientations based on the projector-augmented wave (PAW) method [16,17] using the VASP code [18–21]. In this calculation, we use the same exchange-correlation functional and the $U_{\rm eff}$ parameters as those used in the calculations of XAS and XMCD spectra; however, the SOC is not taken into account.

III. RESULTS AND DISCUSSION

A. Density of states

The calculated total and site-decomposed density of states (DOS) for CCFSO with GGA and GGA + U are shown in Fig. 2. The band gaps (2.65 eV for the spin-up channel and 2.05 eV for the spin-down channel) from GGA + U are about four times wider than those from GGA (0.63 eV for the spin-up channel and 0.58 eV for the spin-down channel). The GGA + U approach is considered essential in this system since the resistivity of CCFSO is too high to measure in the experiment [1]. In the partial DOS of Ca [Figs. 2(a) and 2(b)], there are no valence states around the Fermi level ($E_{\rm F}$) and a large number of states consisting of Ca 3d and 4s orbitals in the conduction band far above $E_{\rm F}$, which means that Ca^{2+} is almost purely ionic in CCFSO. In the Cu DOS, there is an unoccupied $d_{x^2-y^2}$ state in the spin-up channel due to the strong hybridization between the ligand O in the CuO_4 plane, indicating a Cu^{2+} ($3d^9$) configuration as expected from experimental measurement with the bond valence sum (BVS) method [1]. The octahedral surrounding of Fe by O splits the Fe 3d orbitals into t_{2g} and e_g states. The spin-up band in the lower side of the $E_{\rm F}$ and the spin-down band in the upper side of the $E_{\rm F}$ are completely divided by Hund's coupling; therefore, the Fe^{3+} ($3d^5$) assignment is reasonable. The net spin direction of Fe is opposite to that of Cu, indicating stable Cu-Fe ferrimagnetic ordering in CCFSO. In the partial DOS of

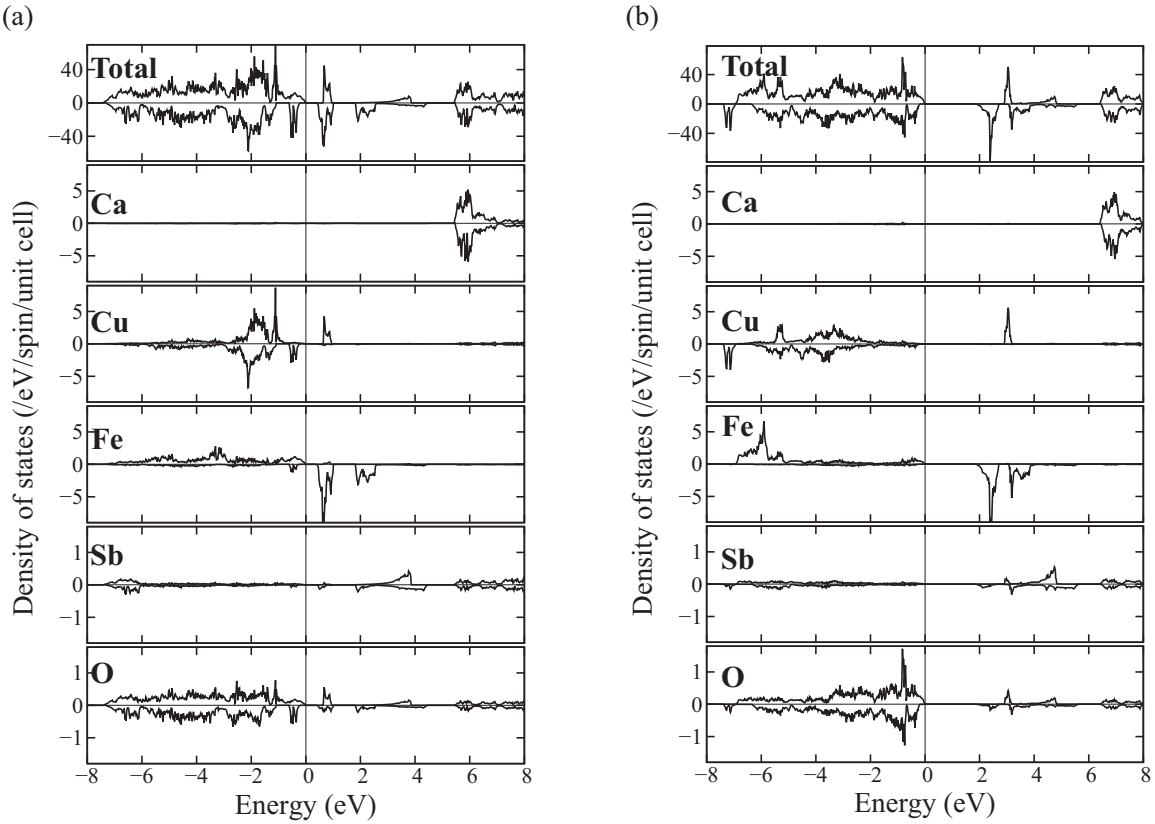

FIG. 2. Total and site-decomposed density of states of $CaCu_3Fe_2Sb_2O_{12}$: (a) GGA and (b) GGA + U + SOC ($U_{\text{eff}} = 7$ eV for Cu and $U_{\text{eff}} = 4$ eV for Fe) with quantization axis [001].

Sb, the conduction band, which mainly consists of the 5s state, is weakly hybridized with the O(2p) band (note the scale).

B. Magnetic moments

The calculated spin and orbital magnetic moments and the spin magnetic dipoles of Cu^{2+} and Fe^{3+} ions are summarized in Table I. The calculated total moment of 7.0 μ_B is in agreement with a nominal value, i.e., an expected ferrimagnetic alignment of $Cu^{2+}(S = 1/2 \downarrow)$ and $Fe^{3+}(S = 5/2 \uparrow)$. The experimentally observed saturation magnetization 5.7 μ_B can be understood by considering the possible existence of anti-site disordering at the B site, i.e., Fe^{3+} is replaced with Sb^{5+} in a ratio of 7.7% and vice versa [1]. In GGA + U calculation with inclusion of SOC, the crystallographically equivalent Cu sites are divided into two sites, Cu1 and Cu2 [see Fig. 1(b)]. The Cu1 (Cu2) site is defined as Cu in the CuO_4 square plane perpendicular (parallel) to the supposed quantization axis [001]. Although the spin magnetic moments of Cu1 and Cu2 are almost equal, the orbital magnetic moments are quite different, i.e., the orbital magnetic moment of Cu1 (-0.14 μ_B) is relatively large and corresponds to about 20% of the spin moments, whereas that of Cu2 (-0.05 μ_B) is much smaller. Furthermore, the spin magnetic dipole $\langle T_z \rangle$ of Cu1 is also twice as large as that of Cu2. These differences are due to the uniaxial symmetry of CuO_4 square planes and the quantization axis dependence of the orbital magnetic moment and spin magnetic dipole [10,22]. The site averaged value of the calculated orbital magnetic moments -0.08 $\mu_B = [(-0.14\ \mu_B) \times 1 + (-0.05\ \mu_B) \times 2]/3$ is equivalent to the experimentally observed value of -0.07 μ_B, even though it is difficult to distinguish the orbital magnetic moment of Cu1 and Cu2 in the experiment. In $Fe^{3+}(3d^5)$, the calculated $\langle L_z \rangle$ and $\langle T_z \rangle$ are both negligibly small because of the highly

TABLE I. Spin and orbital magnetic moments and spin magnetic dipole of Cu and Fe in CCFSO. Spin-quantization axis in SOC calculation is assumed to be along the [001] direction. Cu1 (Cu2) indicates Cu ion in a perpendicular (parallel) CuO_4 plane to spin-quantization axis.

	GGA	GGA + U	GGA + U + SOC		
	$2\langle S_z \rangle$	$2\langle S_z \rangle$	$2\langle S_z \rangle$	$\langle L_z \rangle$	$\langle T_z \rangle$
Cu1	−0.48	−0.73	−0.73	−0.14	−0.19
Cu2		−0.73	−0.72	−0.05	0.09
Fe	3.75	4.08	4.07	0.01	−0.00
Total	7.00	7.00	7.00		
Cu[a]	−0.51	−0.7			
Fe[a]	3.85	4.17			
Total[a]	6.17	6.17			
			Experiment		
Cu[b]			−1.20	−0.07	
Fe[b]			4.63	−0.02	
Total[c]			5.7		

[a]FLAPW calculations [5].
[b]XMCD measurements at 15 K [1].
[c]Field-dependent magnetization measurements at 5 K [1].

symmetric octahedral coordination and isotropic orbital of the $3d^5$. Thus, in terms of the orbital magnetic moments, the calculated values are in good agreement with the experimental values for both Cu and Fe. On the other hand, the calculated spin magnetic moments of Cu ($-0.73\ \mu_B$) and Fe ($4.07\ \mu_B$) are both smaller than those of the experimental values, Cu ($-1.2\ \mu_B$) and Fe ($4.63\ \mu_B$), although our values are in good agreement with those of previous calculations in both GGA and GGA + U in Table I. This discrepancy is thought to be due to the overestimation of the experimental spin magnetic moment obtained from XAS and XMCD measurements through the so-called spin sum rule [23–26]. The spin (and orbital) sum rule requires several assumptions, such as the number of valence holes and the entire absorption caused by target atoms, which are usually difficult to measure accurately. In Ref. [1], the number of valence holes was simply assumed to be 1.0 and 5.0 for $Cu^{2+}(3d^9)$ and $Fe^{3+}(3d^5)$, respectively. According to our calculations, however, the number of holes in the muffin-tin sphere for Cu and Fe $3d$ states are estimated to be 0.73 and 4.43, respectively. By substituting these values into the spin sum rule, the spin magnetic moments are reduced to $-0.88\ \mu_B$ for Cu and $4.10\ \mu_B$ for Fe, which are close to the theoretical values. The expectation value of the spin magnetic dipole $\langle T_z \rangle$ is also required in the spin sum rule. However, in the measurement of powder or polycrystalline samples with weak SOC, the contribution of the spin magnetic dipoles at a high symmetry site, such as O_h and D_{4h}, can vanish due to the angular self-averaging to the incident x ray, i.e., $\langle T_x \rangle + \langle T_y \rangle + \langle T_z \rangle \approx 0$ [27]. Note that the calculated spin magnetic moment of Fe^{3+} ($4.07\ \mu_B$) in CCFSO is larger than that of Fe^{3+} ($3.79\ \mu_B$) in the charge-disproportionate $CaCu_3Fe_2^{3+}Fe_2^{5+}O_{12}$ (Ref. [10]) due to the interruption of the delocalization of Fe^{3+} by the nonmagnetic Sb^{5+} introduced at the Fe^{5+} site in CCFO.

C. XAS and XMCD

In this section, we compare calculated XMCD spectra directly with the experimental ones, instead of comparing the magnetic moments, to avoid the uncertainty in the sum rules discussed above. Figure 3 shows the site-averaged XAS and XMCD spectra for Cu $L_{3,2}$, Fe $L_{3,2}$, and O K edges by assuming magnetization direction along [001]. Compared with the experiment [1], our calculations underestimate the photon energy by about 20 eV for all species because they ignore the core-hole potential, which weakens the screening of the nuclear Coulomb attraction. In the Cu $L_{3,2}$ edges [Fig. 3(a)], the XAS and XMCD spectra show very sharp and nearly structureless peaks at both $L_{3,2}$ edges because there is only one valence-hole in the $3d$ final state. This is in good agreement with those from the experiment. The XMCD spectra are positive at the L_3 edge and negative at the L_2 edge and both weights are slightly different, implying the presence of a finite size of the orbital magnetic moment of Cu. The XMCD intensities of the Cu $L_{3,2}$ edges are opposite in sign to those of the Fe $L_{3,2}$ edges [Fig. 3(b)], indicating the antiferromagnetic coupling between Cu and Fe spins. The XMCD in Fig. 3(b) shows relatively broad peaks at both $L_{3,2}$ edges and they are very similar in shape and weight except that the sign is opposite. This is not consistent with the experiment,

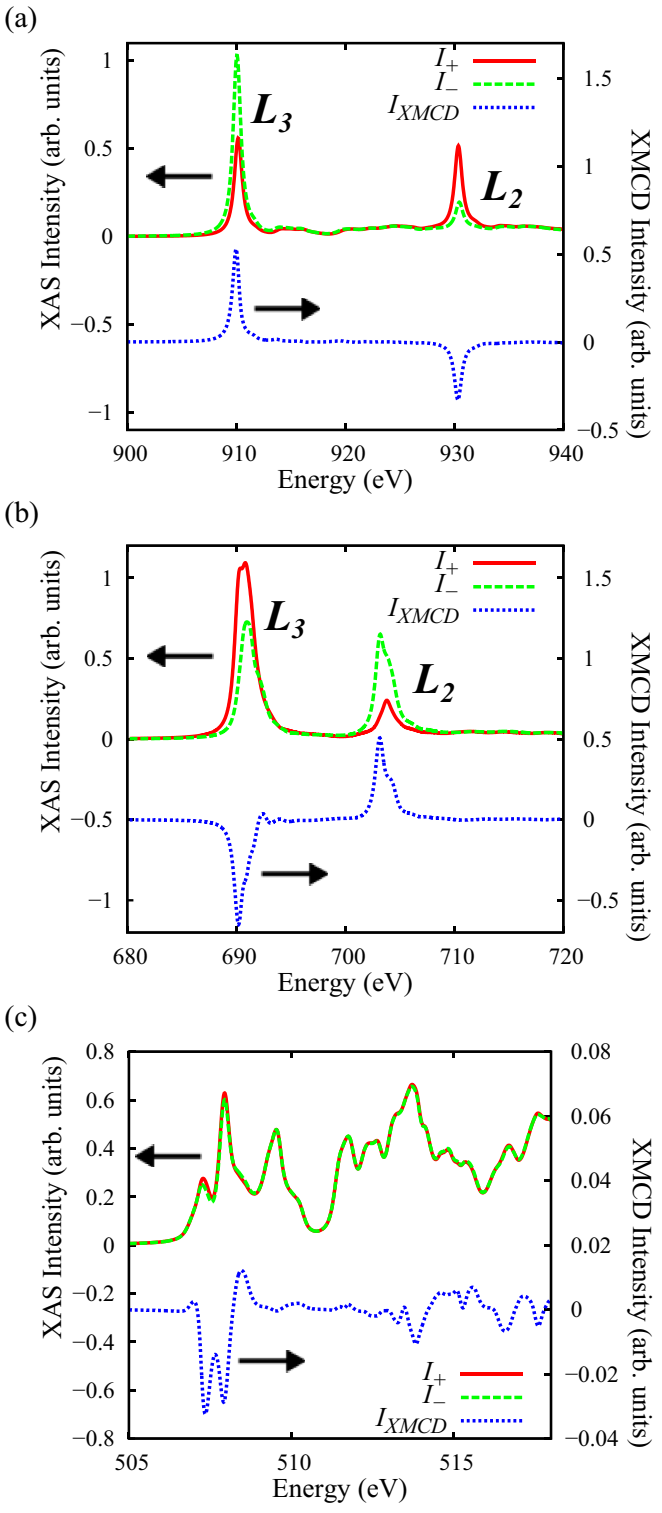

FIG. 3. (Color online) Calculated XAS and XMCD spectra at (a) Cu $L_{3,2}$, (b) Fe $L_{3,2}$, and (c) O K edges with Lorentzian function with widths of 0.4, 0.4, and 0.14 eV, respectively. Red solid (green dashed) lines denote XAS spectra for helicity +(−). Blue dotted lines represent the XMCD spectrum.

in which the shape of the Fe L_2-edge peak is almost squashed compared to that of the L_3 edge [1]. This discrepancy, which can also be seen in the Fe $L_{3,2}$ edges in CCFO [10], may be due to the effect of the multiplet structure, which was not taken

into account in our calculations. In addition, the ignoring of the core-hole might also be responsible for the discrepancy, because the $3d$ valence states are localized in a muffin-tin sphere and can be strongly affected by the core-hole potential. However, the integral of the XMCD spectrum is almost zero, as in the experiment, indicating the quenching of the orbital magnetic moment of Fe^{3+} ($3d^5$). We also calculated the XAS and XMCD of the O K edge, as shown in Fig. 3(c), even though the experimental analysis of the O K edge is very difficult due to the weak intensity. The origin of the XMCD spectrum is due to the small difference between $m = \pm 1$ states in O-$2p$ DOS induced by the strong hybridization with spin-polarized $3d$ bands. The two negative peaks in the region of photon energy of about 507–508 eV corresponds to the hybridized $2p$ state with t_{2g} and e_g states of Fe [see the partial DOS of Fe and O in Fig. 2(b)]. In this case, the effect of ignoring the core-hole is expected to be small because the O-$2p$ orbital of the final state is relatively delocalized.

Since the sign and weight of the experimental XMCD at the Cu and Fe $L_{3,2}$ edges are qualitatively reproduced in our calculations, we can confirm that the ground state in CCFSO is correctly assigned: the antiferromagnetic Cu-Fe and the ferromagnetic Cu-Cu and Fe-Fe couplings. Moreover, the $2p$-$3d$ hybridization observed in the O K-edge spectrum implies the magnetic couplings between Cu and Fe can be described by the superexchange mechanism via O-$2p$ orbitals. In the following sections, we clarify the microscopic origin of the Cu-Fe ferrimagnetism in CCFSO.

D. Exchange couplings

First we calculate the magnetic exchange coupling constants J_{ij} between the local magnetic moments of Cu^{2+} and Fe^{3+} ions. The magnetic energy for a given spin structure is mapped onto an effective classical Heisenberg Hamiltonian as follows:

$$E = -\sum_{i<j} J_{ij} \boldsymbol{e}_i \cdot \boldsymbol{e}_j, \tag{3}$$

where $\boldsymbol{e}_i$ ($\boldsymbol{e}_j$) is the unit vector pointing in the direction of the local magnetic moment at a magnetic site i (j). We focus only on the nearest-neighbor exchange coupling constants for Cu-Cu, Fe-Fe, and Cu-Fe pairs, denoted as J^{CuCu}, J^{FeFe}, and J^{CuFe}, respectively. Equation (3) is then approximated by

$$E \approx -n^{\mathrm{CuCu}} J^{\mathrm{CuCu}} - n^{\mathrm{FeFe}} J^{\mathrm{FeFe}} - n^{\mathrm{CuFe}} J^{\mathrm{CuFe}}, \tag{4}$$

where n are the effective numbers of magnetic pairs in CCFSO, i.e., the difference between the total number of parallel and antiparallel pairs in a given spin structure. The difference in the magnetic energies between different spin structures is reflected only to the n. In other words, we assume the J parameters are configuration-independent constants. In the above approximation, the contributions from further long-range and many-body interactions are renormalized in the J parameters. We consider five different types of magnetic structures as shown in Fig. 4. For calculation of J^{CuCu} and J^{FeFe}, the spin orientations of Cu^{2+} and Fe^{3+} are set to be perpendicular to each other so that the Cu-Fe interactions can be negligible [Figs. 4(a)–4(c)]. The total energies for the given spin configurations are summarized in Table II.

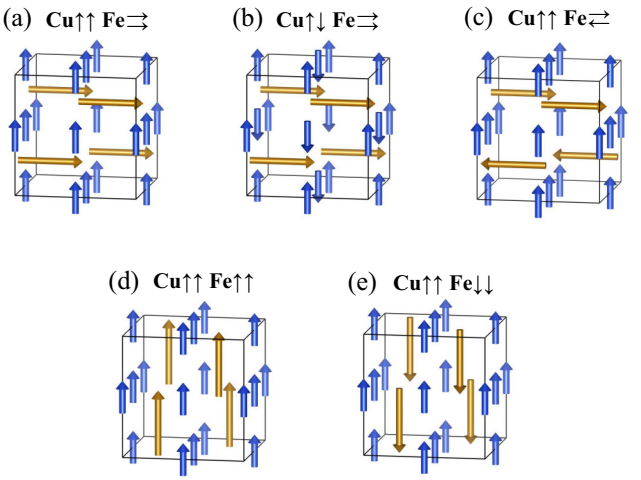

FIG. 4. (Color online) Magnetic structures in unit cells of CCFSO. Short (long) arrows indicate local spin magnetic moment of Cu^{2+} (Fe^{3+}).

The experimentally observed configuration, labeled (e) in Fig. 4 and Table II, has a lower energy than any other magnetic configurations, as expected. From Eq. (4), the magnetic energies of the given magnetic configurations can be described as

$$\begin{aligned} E(a) &= -12J^{\mathrm{CuCu}} - 24J^{\mathrm{FeFe}}, \\ E(b) &= 12J^{\mathrm{CuCu}} - 24J^{\mathrm{FeFe}}, \\ E(c) &= -12J^{\mathrm{CuCu}} + 8J^{\mathrm{FeFe}}, \\ E(d) &= -12J^{\mathrm{CuCu}} - 24J^{\mathrm{FeFe}} - 24J^{\mathrm{CuFe}}, \\ E(e) &= -12J^{\mathrm{CuCu}} - 24J^{\mathrm{FeFe}} + 24J^{\mathrm{CuFe}}. \end{aligned} \tag{5}$$

The J parameters can be extracted from the energy differences between the ferromagnetic and antiferromagnetic configurations, ΔE, as follows:

$$\begin{aligned} \Delta E^{\mathrm{CuCu}} &\equiv E(\mathrm{b}) - E(\mathrm{a}) = 24J^{\mathrm{CuCu}}, \\ \Delta E^{\mathrm{FeFe}} &\equiv E(\mathrm{c}) - E(\mathrm{a}) = 32J^{\mathrm{FeFe}}, \\ \Delta E^{\mathrm{CuFe}} &\equiv E(\mathrm{e}) - E(\mathrm{d}) = 48J^{\mathrm{CuFe}}. \end{aligned} \tag{6}$$

The calculated energy differences and the magnetic coupling constants are summarized in Table III. As shown in Table III, J^{CuCu}, J^{FeFe}, and J^{CuFe} are moderate ferromagnetic (4.93 meV), weak antiferromagnetic (−2.40 meV), and strong antiferromagnetic (−9.81 meV) couplings, respectively, and the absolute J values are inversely related to the pair length d.

TABLE II. Calculated total energies E_{tot} for different magnetic structures labeled as in Fig. 4.

	(a) Cu↑↑ Fe⇉	(b) Cu↑↓ Fe⇉	(c) Cu↑↑ Fe⇄	(d) Cu↑↑ Fe↑↑	(e) Cu↑↑ Fe↓↓
E_{tot} (eV)	−229.240	−229.122	−229.309	−229.012	−229.483

TABLE III. Calculated energy differences ΔE and exchange coupling constants J. d is the nearest-neighbor distance between magnetic pairs.

Label	ΔE (eV)	J (meV)	d (Å)
Cu-Cu	0.118	4.93	3.75
Fe-Fe	−0.077	−2.40	5.31
Cu-Fe	−0.471	−9.81	3.25

Such a weak antiferromagnetic coupling between Fe^{3+}-Fe^{3+} has been observed in double (B-site-ordered) perovskite Ca_2FeSbO_6 (CFSO) with a magnetic transition temperature of $T_N = 17$ K (Ref. [2]). In this case, the antiferromagnetic exchange coupling originates from the long-distance super-superexchange interaction via the empty $5s$ shell of $Sb^{5+}(4d^{10})$ ions along the Fe-O-Sb-O-Fe path. Due to the long distance of Fe-Fe pairs, the exchange coupling constant is very weak. The Cu-Cu ferromagnetism has also been observed in A-site-ordered perovskites CCBO with nonmagnetic B-site ions, such as $CaCu_3Ge_4^{4+}(3d^{10})O_{12}$ and $CaCu_3Sn_4^{4+}(4d^{10})O_{12}$ with $T_C = 13$ K and 10 K, respectively [28], in which the ferromagnetic coupling of Cu-Cu is described as Goodenough-Kanamori-like pictures [29,30] via the Cu1($d_{x^2-y^2}$)-O(p)-Cu2($d_{x^2-y^2}$) superexchange path [11]. The low Curie temperatures of CCBO imply the essentially weak ferromagnetic exchange coupling between Cu ions. To explain the relatively high magnetic transition temperature of $T_C = 170$ K of CCFSO, therefore, it is expected that the magnetic exchange coupling between Cu-Fe must be strong, as calculated above.

Note that the Cu-Fe ferrimagnetic ground state in CCFSO, as observed with XMCD, is a corollary of the consistent spin ordering under the obtained J parameters, i.e., the strong antiferromagnetic J^{CuFe} and following ferromagnetic J^{CuCu} force the Fe spins to align ferromagnetically, even though it is unfavorable for Fe (J^{FeFe} is negative), and the ground-state spin structure of Fig. 4(e) is possible. The J^{FeFe} should no longer be relevant in determining the ground-state spin structure and, by the same reason, the spin-glass behavior is not observed in CCFSO.

The same argument may also be applied to charge-disproportionate $CaCu_3Fe_4O_{12}$ (CCFO). In CCFO, the Cu-Fe ferrimagnetic ground state is possible due to the strong antiferromagnetic Cu-Fe^{3+} couplings and additional antiferromagnetic Cu-Fe^{5+} couplings with weak ferromagnetic Cu-Cu and antiferromagnetic Fe-Fe couplings at temperatures below 210 K [3,4]. In this system, we should understand the meaning of the temperature of 210 K not as the magnetic transition temperature but as the transition temperature of charge disproportionation and if the charge-disproportionate state is not broken even at high temperatures, we can expect that the magnetic transition temperature to be much higher. This might be one of the motivations for the synthesis of CCFSO, which has a robust Fe^{3+} and Sb^{5+} configuration.

E. Ferrimagnetic transition temperature

From J parameters, the T_C of CCFSO is estimated within the mean-field approximation (MFA). In the case of a ferrimagnetic system that has oppositely magnetized sublattices with different magnetization, namely, A (for Cu^{2+}) and B (for Fe^{3+}), T_C is given by

$$T_C = \frac{1}{3k_B}\frac{\tilde{J}^{AA} + \tilde{J}^{BB} + \sqrt{(\tilde{J}^{AA} - \tilde{J}^{BB})^2 + 4\tilde{J}^{AB}\tilde{J}^{BA}}}{2}, \tag{7}$$

where k_B is the Boltzmann constant and the $\tilde{J}$ represent the effective exchange interactions of the magnetic moment at a site on the A or B sublattice [31,32]. The $\tilde{J}$ are determined by the calculated J parameters as follows:

$$\begin{aligned}
\tilde{J}^{AA} &= \sum_{A'(\neq A)} J^{AA'} = 4J^{CuCu},\\
\tilde{J}^{AB} &= \sum_{B'} J^{AB'} = 4J^{CuFe},\\
\tilde{J}^{BB} &= \sum_{B'(\neq B)} J^{BB'} = 12J^{FeFe},\\
\tilde{J}^{BA} &= \sum_{A'} J^{BA'} = 6J^{CuFe},
\end{aligned} \tag{8}$$

where the variable A' (B') indicates a site on the A (B) sublattice and the sum is taken for all nearest neighbors on the sublattice. From Eqs. (7) and (8) and the J parameters listed in Table III, we obtain $T_C = 191$ K, which is in good agreement with the experimental value ($T_C = 170$ K). This indicates that the J parameters seem to be estimated successfully within the present framework. For more accurate estimation for T_C, the random phase approximation or the Monte Carlo approach should be used instead of the MFA.

F. Superexchange mechanism

To understand the mechanisms of the strongest magnetic exchange coupling between Cu and Fe, the orbital-decomposed partial DOS and the spin density are calculated using the FLAPW method. We focus on the empty states at a few eV above E_{VBM} since the superexchange interaction originates from singlet-triplet splitting in the excited states [33]. The partial DOS for Cu, O, and Fe in Fig. 2(b) are decomposed and projected into the orbital-decomposed partial DOS, as shown in Figs. 5(a) and 5(b). The positions of the ions and the principal axes of the orbitals of Cu, O, and Fe are also illustrated in Figs. 5(c) and 5(d).

As can be seen in Fig. 5(a) at around the $E_{VBM} + 3$ eV region in the spin-up channel, the Cu($d_{x^2-y^2}$) orbital is mixed only with the ligand O(p_x) orbital via $pd\sigma$-type hybridization due to the uniaxial CuO_4 symmetry. Furthermore, the O(p_x) orbital is also hybridized with the Fe(t_{2g}) orbital in Fig. 5(b) at around the $E_{VBM} + 2.5$ eV region in the spin-down channel via $pd\pi$-type hybridization. This situation is clearly illustrated in Fig. 6. The figure shows the sum of the square of the absolute value of the wave function within the energy range from $E_{VBM} + 2$ eV to $E_{VBM} + 3$ eV in Fig. 2(b), which corresponds to the upper Hubbard band consisting mainly of the hybridized Cu($d_{x^2-y^2}$), O(p), and Fe(t_{2g}) bands. This figure clearly shows the spin-up polarized (blue) orbital of Cu($d_{x^2-y^2}$), corresponding to the DOS in Fig. 5(a), at an energy

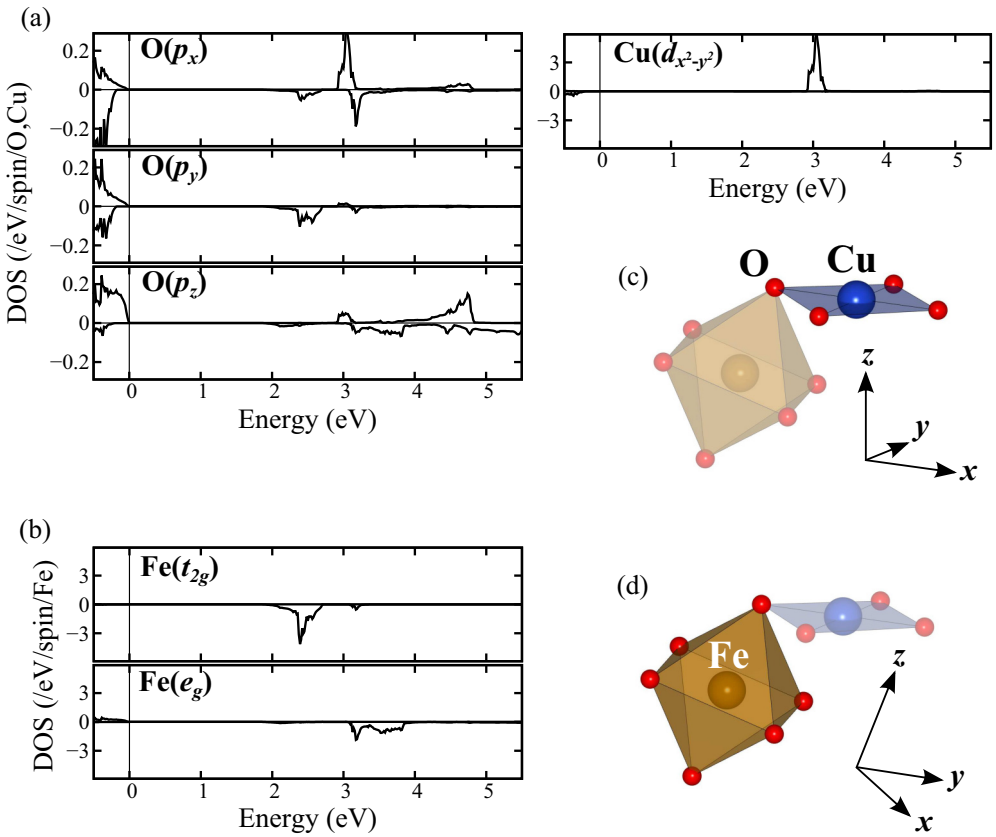

FIG. 5. (Color online) Orbital-decomposed partial density of states of (a) O(p_x, p_y, p_z) and Cu($d_{x^2-y^2}$) and (b) Fe(t_{2g},e_g). Positions of ions and principal axes of orbitals are shown in (c) for O and Cu and (d) for Fe.

range around $E_{\mathrm{VBM}} + 3$ eV, and the spin-down polarized (red) Fe(t_{2g}) orbitals, corresponding to the DOS in Fig. 5(b), at an energy range around $E_{\mathrm{VBM}} + 2.5$. The spin-compensated (green) O(p_x) orbital can also be seen in Fig. 6.

From Figs. 5 and 6, the strong antiferromagnetic coupling between Cu-Fe is interpretable as the superexchange interaction via the Cu($d_{x^2-y^2}$)-O(p_x)-Fe(t_{2g}) exchange path, i.e., based on the hole picture, a perturbed state, Cu-O($p_x^{\uparrow} p_x^{\downarrow}$)-Fe,

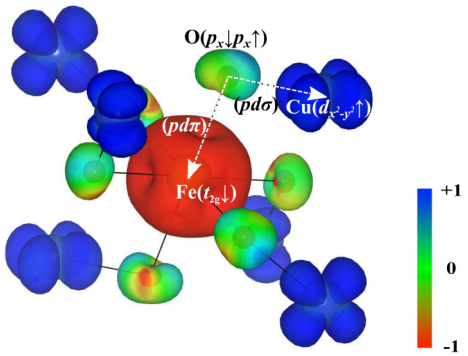

FIG. 6. (Color online) Magnetization density of CCFSO for the Cu($d_{x^2-y^2}$)-O(p_x)-Fe(t_{2g}) band within an energy range from about $E_{\mathrm{VBM}} + 2$ to $E_{\mathrm{VBM}} + 3$ eV in Fig. 2(b). Spin magnetization is described by surface coloring; blue and red regions present up- and down-spin polarized charge density, respectively, and the green region indicates spin-compensated charge density.

can be taken only when the holes have antiparallel spins like Cu($d^{\uparrow}_{x^2-y^2}$) and Fe($t^{\downarrow}_{2g}$) in the ground state. One of the reasons this superexchange coupling is stronger than the others can be attributed to the short distance of the Cu-Fe pairs ($d^{\mathrm{CuFe}} = 3.25$ Å). Note that this superexchange mechanism cannot be sensitive to the choice of the U_{eff} parameters within ranges of $U_{\mathrm{eff}} = 4$–7 eV for Cu and $U_{\mathrm{eff}} = 3$–4 eV for Fe, which are common choices for first-principles studies of transition-metal oxides, because the change in U_{eff} just systematically shifts the positions of the hybridized states of Cu($d_{x^2-y^2}$)-O(p_x) and O(p_x)-Fe(t_{2g}).

IV. SUMMARY

The electronic structure, magnetism, and XMCD spectra of A- and B-site-ordered quadruple perovskite CCFSO was studied from first-principles calculations within GGA + U + SOC. By the inclusion of SOC, we calculated the orbital magnetic moments and spin magnetic dipoles of Cu and Fe in CCFSO as well as the spin magnetic moments. The orbital magnetic moments of Cu and Fe were consistent with the experimental values from XMCD measurements at the $L_{3,2}$ edges via the orbital sum rule. On the other hand, the spin magnetic moments of Cu and Fe were both underestimated. This discrepancy might be caused by inaccuracy in the experimental estimation, namely, the uncertainty of the number of valence holes in the spin sum rules. The XMCD spectra calculations allowed us to compare directly with experimental observations

without any inaccuracy in the sum rules. The sign and weight of the experimental XMCD of the Cu and Fe $L_{3,2}$ edges were qualitatively reproduced. From these calculations, the electronic and magnetic configurations of CCFSO at the ground state were confirmed.

The calculation of the magnetic exchange coupling constants J revealed that the magnetic couplings of Cu-Cu, Fe-Fe, and Cu-Fe are moderate ferromagnetic, weak antiferromagnetic, and strong antiferromagnetic, respectively. This trend is consistent with the $T_{C,N}$ data of CCFSO and its parent compounds, i.e., A-site-ordered perovskite $CaCu_3B_4O_{12}$ (B =Ge and Sn) has low T_C around 10 K and double perovskite Ca_2FeSbO_6 has $T_N = 17$ K, which imply the weak Cu-Cu and Fe-Fe magnetic exchange couplings, respectively. Therefore, the relatively high Curie temperature of CCFSO, $T_C = 170$ K, indicates strong Cu-Fe magnetic exchange coupling. The validity of the calculated J parameters were also confirmed by the consistency in the T_C between the experiment and MFA estimation.

The microscopic origin of the strong antiferromagnetic coupling was successfully explained as the superexchange interaction via the exchange path of Cu($d_{x^2-y^2}$)-O(p_x)-Fe(t_{2g}). The same mechanism will be observed in other ordered $AA'_3B_2B'_2O_{12}$ insulators with magnetic A' and B ions and nonmagnetic B' ions, such as a soft-ferrimagnetic insulator $CaCu_3Cr_2^{3+}Sb_2^{5+}O_{12}$ (Ref. [34]), and even in more complicated insulators with magnetic B' ions, such as charge-disproportionate $CaCu_3Fe_2^{3+}Fe_2^{5+}O_{12}$.

ACKNOWLEDGMENTS

We are grateful to Prof. Y. Shimakawa for his helpful correspondence on experimental aspects. H.F. also thanks Dr. K. Yamauchi and Dr. T. Fukushima for their invaluable discussions and computational support. The experimental data (XAS and XMCD) used in the present work were obtained at BL25SU of the SPring-8 (Proposal No. 2012A1006). This work was supported by the CREST program of the Japan Science and Technology Agency.

[1] W. T. Chen, M. Mizumaki, T. Saito, and Y. Shimakawa, Dalton Trans. **42**, 10116 (2013).
[2] P. D. Battle, T. C. Gibb, A. J. Herod, S.-H. Kim, and P. H. Munns, J. Mater. Chem. **5**, 865 (1995).
[3] I. Yamada, K. Tanaka, N. Hayashi, S. Shinohara, M. Azuma, S. Mori, S. Muranaka, Y. Shimakawa, and M. Takano, Angew. Chem. Int. Ed. **47**, 7032 (2008).
[4] M. Mizumaki, W.-T. Chen, T. Saito, I. Yamada, J. P. Attfield, and Y. Shimakawa, Phys. Rev. B **84**, 094418 (2011).
[5] H. Xiang, J. Wang, J. Meng, and Z. Wu, Comput. Mater. Sci. **46**, 307 (2009).
[6] J. P. Perdew, K. Burke, and M. Ernzerhof, Phys. Rev. Lett. **77**, 3865 (1996).
[7] J. P. Perdew, M. Ernzerhof, and K. Burke, Phys. Rev. Lett. **78**, 1396 (1997).
[8] E. Wimmer, H. Krakauer, M. Weinert, and A. J. Freeman, Phys. Rev. B **24**, 864 (1981).
[9] X. Hao, Y. Xu, F. Gao, D. Zhou, and J. Meng, Phys. Rev. B **79**, 113101 (2009).
[10] T. Ueda, M. Kodera, K. Yamauchi, and T. Oguchi, J. Phys. Soc. Jpn **82**, 094718 (2013).
[11] M. Toyoda, K. Yamauchi, and T. Oguchi, Phys. Rev. B **87**, 224430 (2013).
[12] J. L. Campbell and T. Papp, At. Data Nucl. Data Tables **77**, 1 (2001).
[13] T. Oguchi, K. Iwashita, and T. Jo, Phisica B **237**, 374 (1997).
[14] T. Tsumuraya, T. Shishidou, and T. Oguchi, Phys. Rev. B **77**, 235114 (2008).
[15] N. Ishimatsu, T. Shichijo, Y. Matsushima, H. Maruyama, Y. Matsuura, T. Tsumuraya, T. Shishidou, T. Oguchi, N. Kawamura, M. Mizumaki, T. Matsuoka, and K. Takemura, Phys. Rev. B **86**, 104430 (2012).
[16] P. E. Blöchl, Phys. Rev. B **50**, 17953 (1994).
[17] G. Kresse and D. Joubert, Phys. Rev. B **59**, 1758 (1999).
[18] G. Kresse and J. Hafner, Phys. Rev. B **47**, 558(R) (1993).
[19] G. Kresse and J. Hafner, Phys. Rev. B **49**, 14251 (1994).
[20] G. Kresse and J. Furthmüller, Phys. Rev. B **54**, 11169 (1996).
[21] G. Kresse and J. Furthmüller, Comput. Mater. Sci. **6**, 15 (1996).
[22] T. Oguchi and T. Shishidou, Phys. Rev. B **70**, 024412 (2004).
[23] B. T. Thole, P. Carra, F. Sette, and G. van der Laan, Phys. Rev. Lett. **68**, 1943 (1992).
[24] M. Altarelli, Phys. Rev. B **47**, 597 (1993).
[25] T. Jo, J. Phys. Soc. Japan **62**, 1814 (1993).
[26] P. Carra, B. T. Thole, M. Altarelli, and X. Wang, Phys. Rev. Lett. **70**, 694 (1993).
[27] J. Stöhr and H. König, Phys. Rev. Lett. **75**, 3748 (1995).
[28] H. Shiraki, T. Saito, T. Yamada, M. Tsujimoto, M. Azuma, H. Kurata, S. Isoda, M. Takano, and Y. Shimakawa, Phys. Rev. B **76**, 140403 (2007).
[29] J. B. Goodenough, Phys. Rev. **100**, 564 (1955).
[30] J. Kanamori, J. Phys. Chem. Solids **10**, 87 (1959).
[31] A. Aharoni, *Introduction to the Theory of Ferromagnetism* (Oxford Science, Oxford, 2001).
[32] A. I. Liechtenstein, M. I. Katsnelson, V. P. Antropov, and V. A. Gubanov, J. Magn. Magn. Mater. **67**, 65 (1987).
[33] P. W. Anderson, Phys. Rev. **79**, 350 (1950).
[34] S. H. Byeon, S. S. Lee, J. B. Parise, P. M. Woodward, and N. H. Hur, Chem. Mater. **17**, 3552 (2005).